



HAL
open science

Perfectly matched layers for convex truncated domains with discontinuous Galerkin time domain simulations

Axel Modave, Jonathan Lambrechts, Christophe Geuzaine

► To cite this version:

Axel Modave, Jonathan Lambrechts, Christophe Geuzaine. Perfectly matched layers for convex truncated domains with discontinuous Galerkin time domain simulations. *Computers & Mathematics with Applications*, 2017, 73 (4), pp.684-700. 10.1016/j.camwa.2016.12.027 . hal-01378501v2

HAL Id: hal-01378501

<https://hal.science/hal-01378501v2>

Submitted on 20 Jan 2017

HAL is a multi-disciplinary open access archive for the deposit and dissemination of scientific research documents, whether they are published or not. The documents may come from teaching and research institutions in France or abroad, or from public or private research centers.

L'archive ouverte pluridisciplinaire **HAL**, est destinée au dépôt et à la diffusion de documents scientifiques de niveau recherche, publiés ou non, émanant des établissements d'enseignement et de recherche français ou étrangers, des laboratoires publics ou privés.

Perfectly matched layers for convex truncated domains with discontinuous Galerkin time domain simulations*

A. Modave^{†1,2}, J. Lambrechts³, and C. Geuzaine⁴

¹Virginia Tech, Blacksburg, VA, USA

²POEMS (UMR 7231 CNRS-ENSTA-INRIA), ENSTA ParisTech, Palaiseau, France

³Université catholique de Louvain, Belgium

⁴Université de Liège, Belgium

Abstract

This paper deals with the design of perfectly matched layers (PMLs) for transient acoustic wave propagation in generally-shaped convex truncated domains. After reviewing key elements to derive PML equations for such domains, we present two time-dependent formulations for the pressure-velocity system. These formulations are obtained by using a complex coordinate stretching of the time-harmonic version of the equations in a specific curvilinear coordinate system. The final PML equations are written in a general tensor form, which can easily be projected in Cartesian coordinates to facilitate implementation with classical discretization methods. Discontinuous Galerkin finite element schemes are proposed for both formulations. They are tested and compared using a three-dimensional benchmark with an ellipsoidal truncated domain. Our approach can be generalized to domains with corners.

1 Introduction

Nowadays, the numerical resolution of wave-like problems set on infinite or very large domains remains a challenging task. When using classical schemes based on finite difference, finite volume or finite element methods, a common strategy consists in computing the numerical solution only on a truncated domain, and using an adequate treatment at the artificial boundary to preserve the original solution. This treatment is supposed to simulate the outward propagation of signals and perturbations of all kinds generated inside the truncated domain, even if they are not *a priori* known. For this purpose, a lot of artificial boundary conditions, artificial layers and alternative techniques have been developed, studied and used for decades (see *e.g.* the review papers [5, 25, 34, 36, 38, 39, 75] and references therein). Among them, the high-order absorbing boundary conditions [4, 35, 39, 40, 67] and the perfectly matched layers (PMLs) [6, 13, 15, 18, 43, 45, 46, 49] provide treatments of the artificial boundary with arbitrarily-high accuracy.

The PML method has been introduced by Bérenger in the 90s [13] for transient electromagnetic problems, and has been quickly applied to other wave-like problems. With this method, the truncated domain is extended with a layer, where the governing equations are modified in such a way that outgoing waves are damped. In addition, at the interface between the truncated domain and the layer, the outgoing waves are transmitted without any reflection, whatever the angle of incidence. The combination of both these properties made the success of the method.

The key ingredient of the PML method is the set of governing equations defined inside the layer. With Bérenger's strategy, valid for squared and cuboidal truncated domains, the equations are built by splitting the original equations written in Cartesian coordinates, and using specific dissipations terms [13]. In the

*Published in *Computers & Mathematics with Applications* (doi: [10.1016/j.camwa.2016.12.027](https://doi.org/10.1016/j.camwa.2016.12.027))

[†]Corresponding author. E-mail address: axel.modave@ensta-paristech.fr

time-harmonic context, this strategy corresponds to a stretch of the Cartesian coordinates in the complex plane [21, 63], and can be interpreted as a change of the metric [52, 73]. The PML equations then involve complex metric coefficients. In alternative formulations, the original time-harmonic equations are used in the PML without any change, but complex anisotropic material parameters are defined [32, 66, 78]. These PMLs, frequently called uniaxial PMLs, are interpreted as anisotropic material absorbers. Time-dependent formulations can finally be obtained by taking the inverse Fourier transform in time of time-harmonic PML equations, and using convolution products or additional fields. All the above mentioned strategies have been developed in the electromagnetics community in the 90s. During the last 20 years, they have been used and adapted to design PML formulations for increasingly complex problems in various physical contexts, such as aeroacoustics [45–47, 59], geophysical fluid dynamics [53, 60], elastodynamics [7, 8, 11, 20, 24, 56] and quantum mechanics [79].

Most of the PML formulations are written in Cartesian coordinates and only deal with truncated domains that have straight artificial boundaries (*e.g.* squared or cuboidal). However, some problems are naturally written in other coordinate systems and, since the choice of the truncated domains is *a priori* arbitrary, it could be advantageous to take domains with non-classical shapes. This motivated the derivation of PML systems in alternative coordinate systems, firstly with cylindrical and spherical coordinates [22, 23, 61, 69, 70]. Some PML versions dealing with generally-shaped convex domains have been proposed in time-harmonic contexts by Teixeira and Chew [71, 74], Lassas and Somersalo [51, 52], Zschiedrich *et al* [80] and Matuszyk and Demkowicz [55]. Strategies have been presented for time-dependent simulations with non-Cartesian finite difference schemes [64, 68], mixed finite element schemes [29] and discontinuous Galerkin schemes [3, 30] for Maxwell’s equations. Alternative approaches with layers have also been proposed by Guddati *et al* [37] and Demaldent and Imperiale [26] for polygonal domains.

In this paper, we present two PML formulations for transient acoustic problems defined on convex truncated domains with regular curved boundary. Following strategies used in the electromagnetics community, the formulations are obtained using, respectively, a complex stretch of coordinates and complex material properties in the time-harmonic version of the pressure-velocity system. We derive the tensor form of the final time-dependent equations and we provide the explicit definition of the coefficient tensors, which facilitates implementation with classical discretization methods. Finite element implementations based on a discontinuous Galerkin method are then proposed for both formulations and tested by means of three-dimensional numerical simulations.

This paper is organized as follows. In section 2, PML formulations based on the pressure-velocity system are derived in both time-harmonic and time-dependent contexts for generally-shaped convex domains. Section 3 is dedicated to numerical simulations in the time domain. After describing numerical schemes based on a discontinuous Galerkin method, time-dependent formulations are tested and compared by means of a reference three-dimensional benchmark. An illustration of application is finally proposed.

2 Design of PML formulations

In this section, we derive two families of time-harmonic and time-dependent PML formulations for the acoustic wave system

$$\begin{cases} \frac{\partial p}{\partial t} + \rho c^2 \nabla \cdot \mathbf{u} = 0, \\ \frac{\partial \mathbf{u}}{\partial t} + \frac{1}{\rho} \nabla p = 0, \end{cases} \quad (1)$$

where $p(t, \mathbf{x})$ is the pressure, $\mathbf{u}(t, \mathbf{x})$ is the velocity, ρ is the reference density and c is the propagation speed of the medium. The complete original problem consists in finding the fields $p(t, \mathbf{x})$ and $\mathbf{u}(t, \mathbf{x})$ that are governed by system (1) for $t > 0$ and $\mathbf{x} \in \mathbb{R}^d$, with initial conditions given for both fields at $t = 0$. The spatial dimension d is equal to 2 or 3. For the modified problem, the fields are governed by system (1) only inside the truncated domain $\Omega \subset \mathbb{R}^d$, which is surrounded with the PML Σ (see *e.g.* Fig. 1a).

The time-harmonic PML formulations are obtained from the original equations by stretching a spatial coordinate in the complex plane, which introduces a directional damping of waves. In order to deal with

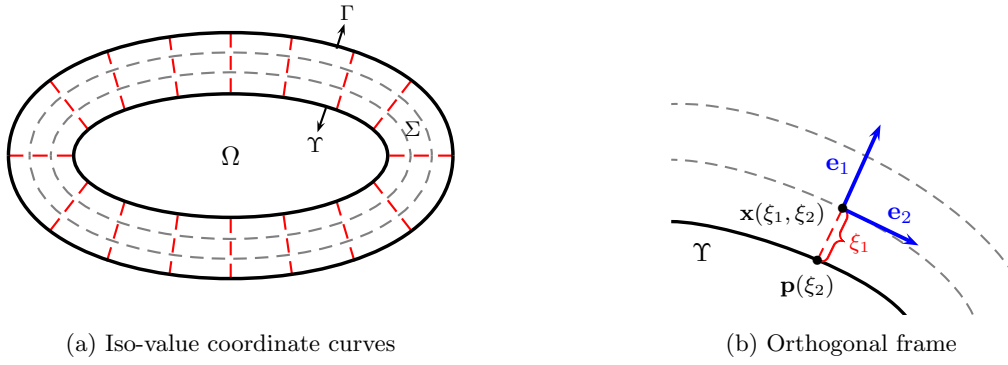


Figure 1: Curvilinear coordinates and local frame associated with the boundary Υ in two dimensions. The curves of iso-value coordinates are represented in Fig. (a). Gray curves are parallel. Red lines are straight and perpendicular to Υ . Fig. (b) shows the local frame and the radial coordinate ξ_1 .

generally-shaped truncated domains, this stretch is performed in a specific local coordinate system. With this strategy, first used by Teixeira and Chew [71], the truncated domain must be convex with a regularity condition on its boundary, and the PML thickness is constant. The time-dependent formulations are then obtained by defining supplementary fields and applying an inverse Fourier transform in time.

The local coordinate system is described in section 2.1. The time-harmonic and time-dependent PML formulations are derived in sections 2.2 and 2.3, respectively.

2.1 Coordinate system associated with the domain boundary

We consider a local coordinate system defined in a layer Σ surrounding the domain Ω with a constant thickness δ . The system is based on lines (in two dimensions) or surfaces (in three dimensions) parallel and perpendicular to the interface Υ (Fig. 1a), which is assumed to be regular enough. This system has been used to derive PMLs [51, 52, 71, 74] and absorbing boundary conditions [4].

In two dimensions, the interface Υ is a curve and the coordinate system is denoted (ξ_1, ξ_2) . Since Ω is convex, each point $\mathbf{x}(\xi_1, \xi_2)$ of the layer Σ has a unique closest point on Υ . We define the coordinate ξ_1 as the distance between the two points, while the coordinate ξ_2 is given by a local parametrization of Υ . We consider a coordinate patch of Υ defined as $\mathbf{p} : \mathcal{V} \subset \mathbb{R} \rightarrow \Upsilon$. Each point of $\mathbf{p}(\mathcal{V}) \subset \Upsilon$ then is given by $\mathbf{p}(\xi_2)$, where $\xi_2 \in \mathcal{V}$. The coordinate patch is chosen in such a way that

$$\frac{d\mathbf{n}}{d\xi_2} = \kappa \mathbf{t}, \quad \text{with } \mathbf{t} = \frac{d\mathbf{p}}{d\xi_2},$$

where $\mathbf{n}(\xi_2)$ is the unit outward normal, $\mathbf{t}(\xi_2)$ is a unit tangent vector and $\kappa(\xi_2)$ is the curvature of Γ at $\mathbf{p}(\xi_2)$. The coordinates ξ_1 and ξ_2 form an orthogonal curvilinear system, and the set of vectors $(\mathbf{e}_1, \mathbf{e}_2) = (\mathbf{n}, \mathbf{t})$ constitutes an orthonormal frame. For each point of the layer Σ , we can then write

$$\mathbf{x}(\xi_1, \xi_2) = \mathbf{p}(\xi_2) + \xi_1 \mathbf{e}_1(\xi_2),$$

which is illustrated in Fig. 1b.

The three-dimensional coordinate system (ξ_1, ξ_2, ξ_3) is adapted from the two-dimensional version. For each point of the layer Σ , the coordinate ξ_1 is the distance with the closest point on the surface Υ , and the coordinates ξ_2 and ξ_3 are provided by a local parametrization of Υ . We consider a coordinate patch $\mathbf{p} : \mathcal{V} \subset \mathbb{R}^2 \rightarrow \Upsilon$. Each point of $\mathbf{p}(\mathcal{V}) \subset \Upsilon$ then is given by $\mathbf{p}(\xi_2, \xi_3)$, where $(\xi_2, \xi_3) \in \mathcal{V}$. There exists a coordinate patch that gives (see [4, 28])

$$\frac{d\mathbf{n}}{d\xi_i} = \kappa_i \mathbf{t}_i, \quad \text{with } \mathbf{t}_i = \frac{d\mathbf{p}}{d\xi_i}, \quad \text{for } i = 2, 3, \quad (2)$$

where $\mathbf{n}(\xi_2, \xi_3)$ is the unit outward normal, $\mathbf{t}_2(\xi_2, \xi_3)$ and $\mathbf{t}_3(\xi_2, \xi_3)$ are two unit tangent vectors in the principal directions and $\kappa_2(\xi_2, \xi_3)$ and $\kappa_3(\xi_2, \xi_3)$ are the principal curvatures of the surface Γ at $\mathbf{p}_2(\xi_2, \xi_3)$. The coordinates ξ_1 , ξ_2 and ξ_3 form an orthogonal curvilinear coordinate system, and the set of vectors $(\mathbf{e}_1, \mathbf{e}_2, \mathbf{e}_3) = (\mathbf{n}, \mathbf{t}_2, \mathbf{t}_3)$ constitutes an orthonormal frame. For each point of the layer Σ , we can then write

$$\mathbf{x}(\xi_1, \xi_2, \xi_3) = \mathbf{p}(\xi_2, \xi_3) + \xi_1 \mathbf{e}_1(\xi_2, \xi_3). \quad (3)$$

In orthogonal curvilinear coordinates, system (1) can be written

$$\left\{ \begin{array}{l} \frac{\partial p}{\partial t} + \rho c^2 \frac{1}{\prod_k h_k} \left(\sum_i \frac{\partial}{\partial \xi_i} \left((\prod_{k \neq i} h_k) u_i \right) \right) = 0, \\ \frac{\partial u_i}{\partial t} + \frac{1}{\rho} \frac{1}{h_i} \frac{\partial p}{\partial \xi_i} = 0, \quad \text{for } i = 1, \dots, d \end{array} \right. \quad (4)$$

where u_i denotes a component of \mathbf{u} in the coordinate system, and h_i is the scale factor associated with the coordinate ξ_i , which is defined by

$$h_i = \left\| \frac{\partial \mathbf{x}}{\partial \xi_i} \right\|. \quad (5)$$

The lower and upper bounds of summation and product symbols are 1 and d , respectively. For the sake of clarity, they are not written. Using the definition (5) together with equations (2) and (3) gives the scale factors for the three-dimensional coordinate system described in this section,

$$\begin{aligned} h_1 &= 1, \\ h_2 &= 1 + \kappa_2(\xi_2, \xi_3) \xi_1, \\ h_3 &= 1 + \kappa_3(\xi_2, \xi_3) \xi_1. \end{aligned}$$

2.2 Coordinate stretch and time-harmonic PML systems

Two PML systems are derived for the time-harmonic acoustic wave system

$$\left\{ \begin{array}{l} -i\omega \hat{p} + \rho c^2 \frac{1}{\prod_k h_k} \left(\sum_i \frac{\partial}{\partial \xi_i} \left((\prod_{k \neq i} h_k) \hat{u}_i \right) \right) = 0, \\ -i\omega \hat{u}_i + \frac{1}{\rho} \frac{1}{h_i} \frac{\partial \hat{p}}{\partial \xi_i} = 0, \quad \text{for } i = 1, 2, 3, \end{array} \right. \quad (6)$$

where ω is the angular frequency and the hat $\hat{\cdot}$ denotes the Fourier transform in time. Both will be used to derive different time-dependent PML formulations in section 2.3.

In a time-harmonic context, a classical way to derive PML systems from the original system consists in stretching one coordinate in the complex plane, where the coordinate corresponds to the direction where waves must be damped in the layer. In our case, this corresponds to replacing the real coordinate $\xi_1 \in [0, \delta]$ with the complex one $\tilde{\xi}_1 \in \mathcal{U}$, where \mathcal{U} is a curve in the complex plane (Fig. 2). We consider the parametrization of the curve

$$\tilde{\xi}_1(\xi_1) = \xi_1 - \frac{1}{i\omega} \int_0^{\xi_1} \sigma(\xi'_1) d\xi'_1, \quad \text{with } \xi_1 \in [0, \delta], \quad (7)$$

where $\sigma(\xi_1)$ is the so-called absorption function, which is positive. The effect of the complex stretching with this specific parametrization can be interpreted by considering the plane wave solution. For the original system (6), the plane wave solution reads

$$e^{i(\mathbf{k} \cdot \mathbf{x} - \omega t)},$$

where the wave number \mathbf{k} is related to the angular frequency through the dispersion relation $\omega = c \|\mathbf{k}\|$. Replacing ξ_1 with $\tilde{\xi}_1$ in this solution gives

$$e^{i(\mathbf{k} \cdot \mathbf{x} - \omega t)} e^{-\gamma(\xi_1)},$$

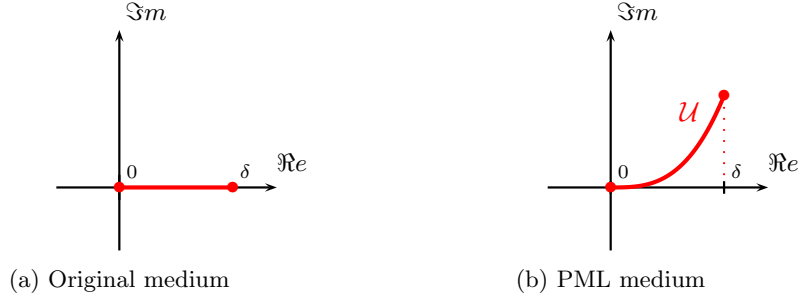


Figure 2: Complex coordinate stretch of the radial coordinate ξ_1 .

with the damping factor

$$\gamma(\xi_1) = \frac{1}{c} \frac{\mathbf{k} \cdot \mathbf{e}_1}{\|\mathbf{k}\|} \int_0^{\xi_1} \sigma(\xi'_1) d\xi'_1.$$

Except grazing waves (*i.e.* $\mathbf{k} \cdot \mathbf{e}_1 = 0$), all the plane waves supported by the original system are damped in their direction of propagation. For outgoing plane waves (*i.e.* $\mathbf{k} \cdot \mathbf{e}_1 > 0$), the damping factor is positive and increases when ξ_1 increases. By contrast, for ingoing plane waves (*i.e.* $\mathbf{k} \cdot \mathbf{e}_1 < 0$), the damping factor is negative and increases when ξ_1 decreases.

When replacing ξ_1 with $\tilde{\xi}_1$ in the time-harmonic system (6), the partial derivative with respect to ξ_1 becomes

$$\frac{\partial}{\partial \xi_1} \rightarrow \frac{\partial}{\partial \tilde{\xi}_1} = \frac{1}{1 - \sigma/(\omega)} \frac{\partial}{\partial \xi_1},$$

and the scale factors h_2 and h_3 , which depend on ξ_1 , become

$$\begin{aligned} h_2 &\rightarrow \tilde{h}_2 = 1 + \kappa_2 \tilde{\xi}_1, \\ h_3 &\rightarrow \tilde{h}_3 = 1 + \kappa_3 \tilde{\xi}_1. \end{aligned}$$

The other partial derivatives do not change, nor does the scale factor $h_1 = 1$. Nevertheless, it is convenient to introduce the complex scale factor defined as $\tilde{h}_1 = 1 - \sigma/(\omega)$. Indeed, the time-harmonic PML system can then be written

$$\begin{cases} -\omega \hat{p} + \rho c^2 \frac{1}{\prod_k \tilde{h}_k} \left(\sum_i \frac{\partial}{\partial \xi_i} \left(\left(\prod_{k \neq i} \tilde{h}_k \right) \hat{u}_i \right) \right) = 0, \\ -\omega \hat{u}_i + \frac{1}{\rho} \frac{1}{\tilde{h}_i} \frac{\partial \hat{p}}{\partial \xi_i} = 0, \quad \text{for } i = 1, 2, 3. \end{cases} \quad (8)$$

An alternative PML system is obtained by defining the new unknowns

$$\hat{u}_i^* = \frac{\prod_{k \neq i} \tilde{h}_k}{\prod_{k \neq i} h_k} \hat{u}_i, \quad \text{for } i = 1, 2, 3.$$

System (8) then becomes

$$\begin{cases} -\omega \hat{p} + \rho c^2 \frac{\prod_k h_k}{\prod_k \tilde{h}_k} \frac{1}{\prod_k h_k} \left(\sum_i \frac{\partial}{\partial \xi_i} \left(\left(\prod_{k \neq i} h_k \right) \hat{u}_i^* \right) \right) = 0, \\ -\omega \hat{u}_i^* + \frac{1}{\rho} \frac{h_i}{\tilde{h}_i} \frac{\prod_{k \neq i} \tilde{h}_k}{\prod_{k \neq i} h_k} \frac{1}{h_i} \frac{\partial \hat{p}}{\partial \xi_i} = 0, \quad \text{for } i = 1, 2, 3. \end{cases} \quad (9)$$

Both time-harmonic PML systems (8) and (9) have interpretations that are well-known in the electromagnetics community. For system (8), the complex coordinate stretch corresponds to a change of the metric

of the space. In an orthogonal coordinate system, the original scale factors h_i are indeed simply replaced with the complex ones \tilde{h}_i (see *e.g.* [52, 73, 74]). The tensor form of system (9) reads

$$\begin{cases} -i\omega\hat{p} + \rho c^2 \alpha \nabla \cdot \hat{\mathbf{u}}^* = 0, \\ -i\omega\hat{\mathbf{u}}^* + \frac{1}{\rho} \mathcal{M} \nabla \hat{p} = 0, \end{cases}$$

where the scalar α and the second-order tensor \mathcal{M} are defined by

$$\alpha = \frac{\prod_k h_k}{\prod_k \tilde{h}_k} \quad \text{and} \quad \mathcal{M} = \sum_i \frac{h_i}{\tilde{h}_i} \frac{\prod_{k \neq i} \tilde{h}_k}{\prod_{k \neq i} h_k} (\mathbf{e}_i \otimes \mathbf{e}_i).$$

This system is identical to the original one (system (1)), except that the (real) material parameters ρc^2 and $1/\rho$ have been replaced with the complex parameter $\rho c^2 \alpha$ and the anisotropic complex tensor \mathcal{M}/ρ . The time-harmonic PML can then simply be interpreted as an anisotropic absorber with specific complex material properties [32, 66, 71]. The same material properties have been obtained for the Helmholtz equation by Matuszyk and Demkowicz [55] in a more general framework.

2.3 Time-dependent PML systems

Two time-dependent PML systems are obtained from the time-harmonic ones (8) and (9) by using an inverse Fourier transform in time. This transform can be performed thanks to the introduction of additional fields and equations. For the sake of clarity, we define the real functions

$$\begin{aligned} \sigma_1 &= \sigma(\xi_1), \\ \sigma_2 &= \bar{\kappa}_2(\xi_1, \xi_2, \xi_3) \bar{\sigma}(\xi_1), \\ \sigma_3 &= \bar{\kappa}_3(\xi_1, \xi_2, \xi_3) \bar{\sigma}(\xi_1), \end{aligned} \tag{10}$$

with

$$\begin{aligned} \bar{\kappa}_i(\xi_1, \xi_2, \xi_3) &= \frac{\kappa_i}{1 + \kappa_i \xi_1}, \quad \text{with } i = 2, 3, \\ \bar{\sigma}(\xi_1) &= \int_0^{\xi_1} \sigma(\xi'_1) d\xi'_1. \end{aligned}$$

These functions allow us to rewrite the complex scale factors as

$$\tilde{h}_i = \left(1 - \frac{\sigma_i}{i\omega}\right) h_i. \tag{12}$$

Let us firstly consider system (8). By using equation (12), the second term of the first equation of system (8) successively becomes

$$\begin{aligned} & \rho c^2 \frac{1}{\prod_k \tilde{h}_k} \sum_i \frac{\partial}{\partial \xi_i} \left(\left(\prod_{k \neq i} \tilde{h}_k \right) \hat{u}_i \right) \\ &= \rho c^2 \frac{1}{\prod_k \tilde{h}_k} \sum_i \left[\left(\prod_{k \neq i} \left(1 - \frac{\sigma_k}{i\omega}\right) \right) \frac{\partial}{\partial \xi_i} \left(\left(\prod_{k \neq i} h_k \right) \hat{u}_i \right) + \left(\prod_{k \neq i} h_k \right) \hat{u}_i \frac{\partial}{\partial \xi_i} \left(\prod_{k \neq i} \left(1 - \frac{\sigma_k}{i\omega}\right) \right) \right] \\ &= \sum_i \left(1 - \frac{\sigma_i}{i\omega}\right)^{-1} \left[\rho c^2 \frac{1}{\prod_k h_k} \frac{\partial}{\partial \xi_i} \left(\left(\prod_{k \neq i} h_k \right) \hat{u}_i \right) \right] + \sum_i \left[\rho c^2 \left(\prod_k \left(1 - \frac{\sigma_k}{i\omega}\right)^{-1} \right) \frac{\hat{u}_i}{h_i} \frac{\partial}{\partial \xi_i} \left(\prod_{k \neq i} \left(1 - \frac{\sigma_k}{i\omega}\right) \right) \right] \\ &= \sum_i \left(1 - \frac{\sigma_i}{\sigma_i - i\omega}\right) \left[\rho c^2 \frac{1}{\prod_k h_k} \frac{\partial}{\partial \xi_i} \left(\left(\prod_{k \neq i} h_k \right) \hat{u}_i \right) \right] + \sum_i \left[\rho c^2 \frac{(-i\omega)}{\sigma_i - i\omega} \sum_{k \neq i} \left[\frac{1}{\sigma_k - i\omega} \frac{\partial \sigma_k}{\partial \xi_i} \right] \frac{\hat{u}_i}{h_i} \right]. \end{aligned}$$

Using the definitions of $\sigma_1, \sigma_2, \sigma_3$ and h_1 , the second term can be simplified as

$$\begin{aligned}
& \sum_i \left[\rho c^2 \frac{(-i\omega)}{\sigma_i - i\omega} \sum_{k \neq i} \left[\frac{1}{\sigma_k - i\omega} \frac{\partial \sigma_k}{\partial \xi_i} \right] \frac{\hat{u}_i}{h_i} \right] \\
&= \rho c^2 \hat{u}_1 \frac{(-i\omega)}{\sigma_1 - i\omega} \left[\frac{1}{\sigma_2 - i\omega} \frac{\partial \sigma_2}{\partial \xi_1} + \frac{1}{\sigma_3 - i\omega} \frac{\partial \sigma_3}{\partial \xi_1} \right] + \rho c^2 \frac{(-i\omega)}{(\sigma_2 - i\omega)(\sigma_3 - i\omega)} \left[\frac{\hat{u}_2}{h_2} \frac{\partial \sigma_3}{\partial \xi_2} + \frac{\hat{u}_3}{h_3} \frac{\partial \sigma_2}{\partial \xi_3} \right] \\
&= \rho c^2 \hat{u}_1 \frac{(-i\omega)}{\sigma_1 - i\omega} \left[\frac{\sigma_1 - \sigma_2}{\sigma_2 - i\omega} \bar{\kappa}_2 + \frac{\sigma_1 - \sigma_3}{\sigma_3 - i\omega} \bar{\kappa}_3 \right] + \rho c^2 \frac{(-i\omega)}{(\sigma_2 - i\omega)(\sigma_3 - i\omega)} \left[\frac{\hat{u}_2}{h_2} \frac{\partial \sigma_3}{\partial \xi_2} + \frac{\hat{u}_3}{h_3} \frac{\partial \sigma_2}{\partial \xi_3} \right] \\
&= \rho c^2 \hat{u}_1 \left[-\frac{(-i\omega)}{\sigma_1 - i\omega} (\bar{\kappa}_2 + \bar{\kappa}_3) + \frac{(-i\omega)}{\sigma_2 - i\omega} \bar{\kappa}_2 + \frac{(-i\omega)}{\sigma_3 - i\omega} \bar{\kappa}_3 \right] + \rho c^2 \frac{(-i\omega) \bar{\sigma}}{(\sigma_2 - i\omega)(\sigma_3 - i\omega)} \left[\frac{\bar{\kappa}_3^2}{\kappa_3^2} \frac{\hat{u}_2}{h_2} \frac{\partial \kappa_3}{\partial \xi_2} + \frac{\bar{\kappa}_2^2}{\kappa_2^2} \frac{\hat{u}_3}{h_3} \frac{\partial \kappa_2}{\partial \xi_3} \right] \\
&= \sum_i \left(1 - \frac{\sigma_i}{\sigma_i - i\omega} \right) (\hat{q}_i + \bar{\sigma} \hat{r}_i),
\end{aligned}$$

where we have introduced the additional fields

$$\begin{aligned}
\hat{q}_1 &= -\rho c^2 (\bar{\kappa}_2 + \bar{\kappa}_3) \hat{u}_1, & \hat{r}_1 &= 0, \\
\hat{q}_2 &= \rho c^2 \bar{\kappa}_2 \hat{u}_1, & \hat{r}_2 &= \rho c^2 \frac{1}{\sigma_3 - i\omega} \frac{\bar{\kappa}_3^2}{\kappa_3^2} \frac{\hat{u}_2}{h_2} \frac{\partial \kappa_3}{\partial \xi_2}, \\
\hat{q}_3 &= \rho c^2 \bar{\kappa}_3 \hat{u}_1, & \hat{r}_3 &= \rho c^2 \frac{1}{\sigma_2 - i\omega} \frac{\bar{\kappa}_2^2}{\kappa_2^2} \frac{\hat{u}_3}{h_3} \frac{\partial \kappa_2}{\partial \xi_3}.
\end{aligned}$$

Defining the additional fields

$$\hat{p}_i = -\frac{1}{\sigma_i - i\omega} \left[\rho c^2 \frac{1}{\prod_k h_k} \frac{\partial}{\partial \xi_i} \left(\left(\prod_{k \neq i} h_k \right) \hat{u}_i \right) + \hat{q}_i + \bar{\sigma} \hat{r}_i \right], \quad \text{for } i = 1, 2, 3,$$

system (8) can be rewritten as

$$\left\{ \begin{aligned}
& -i\omega \hat{p} + \rho c^2 \frac{1}{\prod_k h_k} \left(\sum_i \frac{\partial}{\partial \xi_i} \left(\left(\prod_{k \neq i} h_k \right) \hat{u}_i \right) \right) = -\sum_i (\sigma_i \hat{p}_i) - \sum_i (\hat{q}_i + \bar{\sigma} \hat{r}_i), \\
& -i\omega \hat{u}_i + \frac{1}{\rho} \frac{1}{h_i} \frac{\partial \hat{p}}{\partial \xi_i} = -\sigma_i \hat{u}_i, & \text{for } i = 1, 2, 3, \\
& -i\omega \hat{p}_i + \rho c^2 \frac{1}{\prod_k h_k} \frac{\partial}{\partial \xi_i} \left(\left(\prod_{k \neq i} h_k \right) \hat{u}_i \right) = -(\sigma_i \hat{p}_i + \hat{q}_i + \bar{\sigma} \hat{r}_i), & \text{for } i = 1, 2, 3, \\
& -i\omega \hat{r}_2 = \rho c^2 \frac{\bar{\kappa}_3^2}{\kappa_3^2} \frac{\hat{u}_2}{h_2} \frac{\partial \kappa_3}{\partial \xi_2} - \sigma_3 \hat{r}_2, \\
& -i\omega \hat{r}_3 = \rho c^2 \frac{\bar{\kappa}_2^2}{\kappa_2^2} \frac{\hat{u}_3}{h_3} \frac{\partial \kappa_2}{\partial \xi_3} - \sigma_2 \hat{r}_3.
\end{aligned} \right.$$

One equation can be removed by using $\hat{p} = \sum_i \hat{p}_i$, as well as one term of the first equation since $\sum_i \hat{q}_i = 0$. Using an inverse Fourier transform in time, we finally obtain the time-dependent PML system

$$\left\{ \begin{aligned}
& \frac{\partial p}{\partial t} + \rho c^2 \nabla \cdot \mathbf{u} = -\sigma_1 p_1 - \sigma_2 p_2 - \sigma_3 (p - p_1 - p_2) - \bar{\sigma} (r_2 + r_3), \\
& \frac{\partial \mathbf{u}}{\partial t} + \frac{1}{\rho} \nabla p = -\sum_i \sigma_i u_i \mathbf{e}_i, \\
& \frac{\partial p_i}{\partial t} + \rho c^2 \nabla_i \cdot \mathbf{u} = -\sigma_i p_i - q_i - \bar{\sigma} r_i, \quad \text{for } i = 1, 2, \\
& \frac{\partial r_2}{\partial t} = \rho c^2 u_2 \frac{\bar{\kappa}_3^2}{\kappa_3^2} (\mathbf{e}_2 \cdot \nabla \kappa_3) - \sigma_3 r_2, \\
& \frac{\partial r_3}{\partial t} = \rho c^2 u_3 \frac{\bar{\kappa}_2^2}{\kappa_2^2} (\mathbf{e}_3 \cdot \nabla \kappa_2) - \sigma_2 r_3.
\end{aligned} \right. \quad (13)$$

with $u_i = \mathbf{e}_i \cdot \mathbf{u}$, $q_1 = -\rho c^2(\bar{\kappa}_2 + \bar{\kappa}_3)u_1$, $q_2 = \rho c^2 \bar{\kappa}_2 u_1$ and

$$\nabla_i \cdot \mathbf{u} \stackrel{\text{def.}}{=} \nabla \cdot (u_i \mathbf{e}_i). \quad (14)$$

With this system, the governing equations of p and \mathbf{u} are identical to the original ones, but with additional non-differential terms. The original equations are recovered if σ is equal to zero. This formulation has four supplementary differential equations: two with the differential operator of equation (14) and two ordinary differential equations. The latter involve the spatial variation of each principal curvature (κ_2 and κ_3) in the other principal direction (respectively, \mathbf{e}_3 and \mathbf{e}_2). For a sphere, the curvature is constant and the fields r_1 and r_2 are equal to zero. In two dimensions, only one supplementary partial differential equation is required.

We now consider system (9), which can be rewritten as

$$\begin{cases} -\imath\omega \hat{p} + \rho c^2 \frac{1}{\prod_k h_k} \left(\sum_i \frac{\partial}{\partial \xi_i} \left(\left(\prod_{k \neq i} h_k \right) \hat{u}_i \right) \right) = -\imath\omega \left(1 - \frac{\prod_k \tilde{h}_k}{\prod_k h_k} \right) \hat{p}, \\ -\imath\omega \hat{u}_i + \frac{1}{\rho} \frac{\partial \hat{p}}{h_i \partial \xi_i} = -\imath\omega \left(1 - \frac{\tilde{h}_i \prod_{k \neq i} h_k}{h_i \prod_{k \neq i} \tilde{h}_k} \right) \hat{u}_i. \end{cases}$$

For the sake of clarity, the superscript $*$ has been removed. Using equation (12), the right-hand sides of these equations become

$$\begin{aligned} -\imath\omega \left(1 - \frac{\prod_k \tilde{h}_k}{\prod_k h_k} \right) \hat{p} &= -\imath\omega \left(1 - \left(1 - \frac{\sigma_1}{\imath\omega} \right) \left(1 - \frac{\sigma_2}{\imath\omega} \right) \left(1 - \frac{\sigma_3}{\imath\omega} \right) \right) \hat{p} \\ &= -(\sum_i \sigma_i) \hat{p} - \left(\sum_i \prod_{k \neq i} \sigma_i \right) \frac{\hat{p}}{(-\imath\omega)} - \left(\prod_i \sigma_i \right) \frac{\hat{p}}{(-\imath\omega)^2}, \\ -\imath\omega \left(1 - \frac{\tilde{h}_i \prod_{k \neq i} h_k}{h_i \prod_{k \neq i} \tilde{h}_k} \right) \hat{u}_i &= -\imath\omega \left(1 - \frac{1 - \sigma_i / (\imath\omega)}{\prod_{k \neq i} (1 - \sigma_k / (\imath\omega))} \right) \hat{u}_i \\ &= -\imath\omega \frac{\prod_{k \neq i} (\imath\omega - \sigma_k) - \imath\omega (\imath\omega - \sigma_i)}{\prod_{k \neq i} (\imath\omega - \sigma_k)} \hat{u}_i \\ &= -\imath\omega \frac{\imath\omega (\sigma_i - \sum_{k \neq i} \sigma_k) + \prod_{k \neq i} \sigma_k}{\prod_{k \neq i} (\imath\omega - \sigma_k)} \hat{u}_i \\ &= -(\sigma_i - \sum_{k \neq i} \sigma_k) (\hat{v}_i + \hat{u}_i) - \left(\prod_{k \neq i} \sigma_k \right) \hat{w}_i, \end{aligned}$$

where \hat{v}_i and \hat{w}_i have been introduced such that

$$\begin{aligned} \hat{v}_i + \hat{u}_i &= \frac{(\imath\omega)^2}{\prod_{k \neq i} (\imath\omega - \sigma_k)} \hat{u}_i = \frac{(\imath\omega)^2}{(\imath\omega)^2 - \imath\omega \left(\sum_{k \neq i} \sigma_k \right) + \left(\prod_{k \neq i} \sigma_k \right)} \hat{u}_i, \\ \hat{w}_i &= \frac{\imath\omega}{\prod_{k \neq i} (\imath\omega - \sigma_k)} \hat{u}_i = \frac{\imath\omega}{(\imath\omega)^2 - \imath\omega \left(\sum_{k \neq i} \sigma_k \right) + \left(\prod_{k \neq i} \sigma_k \right)} \hat{u}_i, \end{aligned}$$

which give

$$\begin{aligned} -\imath\omega \hat{v}_i &= -\left(\sum_{k \neq i} \sigma_k \right) (\hat{v}_i + \hat{u}_i) + \left(\prod_{k \neq i} \sigma_k \right) \hat{w}_i, \\ -\imath\omega \hat{w}_i &= -(\hat{v}_i + \hat{u}_i). \end{aligned}$$

Defining supplementary fields for $\hat{p}/(-\imath\omega)$ and $\hat{p}/(-\imath\omega)^2$, and using an inverse Fourier transform in time, we

finally obtain the system

$$\left\{ \begin{array}{l} \frac{\partial p}{\partial t} + \rho c^2 \frac{1}{\prod_k h_k} \left(\sum_i \frac{\partial}{\partial \xi_i} \left(\left(\prod_{k \neq i} h_k \right) u_i \right) \right) = -(\sum_i \sigma_i) p - \left(\sum_i \prod_{k \neq i} \sigma_i \right) p^{(1)} - \left(\prod_i \sigma_i \right) p^{(2)}, \\ \frac{\partial u_i}{\partial t} + \frac{1}{\rho} \frac{1}{h_i} \frac{\partial p}{\partial \xi_i} = -\left(\sigma_i - \sum_{k \neq i} \sigma_k \right) (u_i + v_i) - \left(\prod_{k \neq i} \sigma_k \right) w_i, \\ \frac{\partial p^{(1)}}{\partial t} = p, \quad \frac{\partial v_i}{\partial t} = -\left(\sum_{k \neq i} \sigma_k \right) (u_i + v_i) + \left(\prod_{k \neq i} \sigma_k \right) w_i, \\ \frac{\partial p^{(2)}}{\partial t} = p^{(1)}, \quad \frac{\partial w_i}{\partial t} = -(v_i + u_i). \end{array} \right.$$

The tensor form of this system reads

$$\left\{ \begin{array}{l} \frac{\partial p}{\partial t} + \rho c^2 \nabla \cdot \mathbf{u} = -(\sigma_1 + \sigma_2 + \sigma_3) p - (\sigma_1 \sigma_2 + \sigma_1 \sigma_3 + \sigma_2 \sigma_3) p^{(1)} - (\sigma_1 \sigma_2 \sigma_3) p^{(2)}, \\ \frac{\partial \mathbf{u}}{\partial t} + \frac{1}{\rho} \nabla p = -\mathcal{A}(\mathbf{u} + \mathbf{v}) - \mathcal{B}\mathbf{w}, \\ \frac{\partial p^{(1)}}{\partial t} = p, \quad \frac{\partial \mathbf{v}}{\partial t} = -\mathcal{C}(\mathbf{u} + \mathbf{v}) + \mathcal{B}\mathbf{w}, \\ \frac{\partial p^{(2)}}{\partial t} = p^{(1)}, \quad \frac{\partial \mathbf{w}}{\partial t} = -(\mathbf{u} + \mathbf{v}), \end{array} \right. \quad (15)$$

with the second-order tensors

$$\begin{aligned} \mathcal{A} &= (\sigma_1 - \sigma_2 - \sigma_3) \mathcal{I}_1 + (-\sigma_1 + \sigma_2 - \sigma_3) \mathcal{I}_2 + (-\sigma_1 - \sigma_2 + \sigma_3) \mathcal{I}_3, \\ \mathcal{B} &= (\sigma_2 \sigma_3) \mathcal{I}_1 + (\sigma_1 \sigma_3) \mathcal{I}_2 + (\sigma_1 \sigma_2) \mathcal{I}_3, \\ \mathcal{C} &= (\sigma_2 + \sigma_3) \mathcal{I}_1 + (\sigma_1 + \sigma_3) \mathcal{I}_2 + (\sigma_1 + \sigma_2) \mathcal{I}_3, \end{aligned}$$

where $\mathcal{I}_i = \mathbf{e}_i \otimes \mathbf{e}_i$. As in system (13), p and \mathbf{u} are governed by the original equations where source terms are added. By contrast, this formulation involves two scalar and two vectorial supplementary fields, which are governed by ordinary differential equations. Only one scalar field and one vector field are required in two dimensions.

In the remainder, systems (13) and (15) are respectively called the PML-PDE system and the PML-ODE system.

Interpretation and extension for domains with corners

Though the PML systems have been derived for convex domains with regular boundary, they can straightforwardly be adapted for squared and cuboidal domains with edge and corner regions where layers overlap. Formula (12) is classically used to stretch scale factors in the Cartesian directions to derive PML for squared and cuboidal domains (see *e.g.* [72, 74]). Therefore, the PML systems (13) and (15) can be used as is for Cartesian PMLs, but each absorption function $\sigma_i(x_i)$ is chosen independently and corresponds to the damping of waves in the corresponding Cartesian direction \mathbf{e}_i .

An analogy with the Cartesian PMLs provides a nice interpretation for the absorbing functions σ_2 and σ_3 expressed in equations (10) and (11). They can be considered as absorption functions associated with the principal directions, but they are due to the curvature of the domain boundary. They are equal to zero if the boundary is planar.

The validity of the PML systems (13) and (15) can also be extended to other convex domains having corners with right angles. For instance, they can deal with cylindrical domains having convex cross-sections. Let us consider a cylinder with the axis \mathbf{e}_3 . In the lateral PML that surrounds the cylinder, the PML systems are then simply obtained by considering that κ_2 is the curvature of the cross section and $\kappa_3 \rightarrow 0$ in relations (10) and (11); \mathbf{e}_1 remains the radial direction and \mathbf{e}_2 is tangent the lateral surface and perpendicular to \mathbf{e}_3 . At the two extremities of the cylinder, the PMLs are planar and only σ_3 is non-zero. At the corner, σ_1 and σ_2 are defined as in the lateral PML, and σ_3 is defined as in the PML of the border.

Classification and mathematical properties

The derived PML-PDE system (13) and PML-ODE system (15) can be categorized into two well-known families of PMLs. The first family contains the *Bérenger-like* PML systems that are built using the splitting-field technique of Bérenger [13] or the complex coordinate stretch technique [21, 22]. These systems involve additional fields governed by differential equations with spatial partial derivatives (see *e.g.* [14, 23, 24, 45–47, 60]). The second family corresponds to PML systems based on frequency-dependent complex material properties [32, 66, 78] and written in the time-domain with supplementary ordinary differential equations [2, 19, 62]. Such PMLs are generally referred as *uniaxial* PMLs.

The mathematical properties of PMLs from both families have been studied in many works and are still an active field of research (see *e.g.* [1, 2, 9, 10, 27, 31, 41, 42, 48, 62]). For wave problems described with symmetric hyperbolic systems (*e.g.* acoustic system (1) and Maxwell’s equations), the PML systems derived with the original strategy of Bérenger are weakly hyperbolic, and lead to weakly well-posed problems [1, 9]. By contrast, the uniaxial PML systems are symmetric hyperbolic and lead to strongly well-posed problems [2, 42, 62]. To our knowledge, only proofs of weak stability have been proposed for standard PML systems from both families [9, 12, 19]. This means that no exponentially growing modes are supported by the equations, but linear modes could pollute the solution in long-duration simulations. Since the PML systems studied in [9, 12, 19] correspond to planar versions of systems (13) and (15), the PML formulations proposed in this work will also suffer from the same long-time instability.

Let us note that modified PML formulations have been proposed to avoid any linear growing mode, and to improve the accuracy for problems involving evanescent and grazing waves. For instance, the so-called *complex frequency shifted* PML formulations [50, 65] are derived using a modified coordinate stretch, where new parameters are introduced. In the time domain, these formulations can be seen as generalizations of standard PML formulations with supplementary terms and equations. The formulations proposed in this work could be enriched using the modified coordinate stretch, but at the cost of larger PML systems and more expensive computations.

3 Numerical simulations

Both time-dependent PML formulations are tested by means of a three-dimensional benchmark where a spherical wavefront is propagated in a truncated domain. The computational domain is the half of an ellipsoid of revolution, whose shell is extended with a PML. The simulations are performed using discontinuous finite element schemes that are described in section 3.1. After the description of the benchmark in section 3.2, accuracy results are proposed to validate our implementation and performance results are discussed (section 3.3). An illustration of application is finally proposed in section 3.4.

For the PML-PDE formulation (13), both fields r_i are set to zero and the corresponding equations are not computed. Since the domain has an axis of revolution, one of the principal curvatures is constant, and the corresponding field is equal zero. Setting the other field to zero is an approximation that corresponds to neglecting the effect of the spatial variation of the other principal curvature. With our specific benchmark, we have observed *a posteriori* that the performances of the formulation remain very good in comparison to the PML-ODE formulation, which is implemented without any approximation.

3.1 Discontinuous finite element schemes

We propose numerical schemes based on a nodal discontinuous Galerkin (DG) method for the PML systems. The schemes are derived following a classical strategy for hyperbolic systems [44], with some further developments to discretize the supplementary equations.

The unknown fields are approximated on a spatial mesh of Ω made of non-overlapping polyhedral cells, $\Omega = \bigcup_{k=1, \dots, K} D_k$, where K is the number of cells and D_k is the k^{th} cell. With the nodal DG method, each scalar field and each Cartesian component of vector fields is approximated by piecewise polynomial functions, where discontinuities correspond to interfaces between elements. The discrete unknowns correspond to the

values of fields at the nodes of elements. Over each cell D_k , the approximation of any field $q(\mathbf{x}, t)$ can then be written as

$$q_k(\mathbf{x}, t) = \sum_{n=1}^{N_k} q_{k,n}(t) \ell_{k,n}(\mathbf{x}), \quad \forall \mathbf{x} \in D_k,$$

where N_k is the number of nodes over element k , $q_{k,n}(t)$ is the value of the field at node n , and $\ell_{k,n}(\mathbf{x})$ is the multivariate Lagrange polynomial function associated with node n .

For both the original system (1) and the PML systems (13) and (15), the governing equations of p and \mathbf{u} are discretized in the same manner. Multiplying these equations by test functions \hat{p} and $\hat{\mathbf{u}}$, integrating the resulting equations over any cell D_k , and using integration by parts, we get the weak form

$$\begin{aligned} \left(\frac{\partial p}{\partial t}, \hat{p} \right)_{D_k} - (\rho c^2 \mathbf{u}, \nabla \hat{p})_{D_k} + \langle f_p, \hat{p} \rangle_{\partial D_k} &= (s_p, \hat{p})_{D_k}, \\ \left(\frac{\partial \mathbf{u}}{\partial t}, \hat{\mathbf{u}} \right)_{D_k} - \left(\frac{p}{\rho}, \nabla \cdot \hat{\mathbf{u}} \right)_{D_k} + \langle \mathbf{f}_u, \hat{\mathbf{u}} \rangle_{\partial D_k} &= (\mathbf{s}_u, \hat{\mathbf{u}})_{D_k}, \end{aligned}$$

with the fluxes

$$\begin{aligned} f_p &= \rho c^2 \mathbf{n}_k \cdot \mathbf{u}, \\ \mathbf{f}_u &= \frac{p}{\rho} \mathbf{n}_k, \end{aligned}$$

where \mathbf{n}_k is the outward unit normal on the boundary ∂D_k . For both PML systems, s_p and \mathbf{s}_u contain the right-hand side terms of the governing equations of p and \mathbf{u} . The discrete fields being discontinuous at the interface between elements, the fluxes are replaced by numerical fluxes which involve values of fields from both sides of interfaces. We choose the upwind fluxes

$$f_p^{\text{num}} = \rho c^2 \mathbf{n}_k \cdot \{ \mathbf{u} \} - c \llbracket p \rrbracket, \quad (16)$$

$$\mathbf{f}_u^{\text{num}} = \frac{1}{\rho} \mathbf{n}_k \{ p \} - c \mathbf{n}_k (\mathbf{n}_k \cdot \llbracket \mathbf{u} \rrbracket), \quad (17)$$

where the mean $\{q\}$ and the semi-jump $\llbracket q \rrbracket$ of any field q are defined as

$$\begin{aligned} \{q\} &= \frac{q^+ + q^-}{2}, \\ \llbracket q \rrbracket &= \frac{q^+ - q^-}{2}. \end{aligned}$$

The plus and minus subscripts denote values on the side of the neighboring and current cells, respectively. These fluxes are classically obtained by using a Riemann solver (see *e.g.* [44, 54]). At the external boundary, we use a first-order absorbing boundary condition (ABC) based on characteristics, which is simply implemented by taking the external values p^+ and \mathbf{u}^+ equal to zero in the numerical fluxes (16)-(17).

For the PML-PDE system (13), the partial differential equations that govern the supplementary fields p_1 and p_2 are discretized by analogy with the governing equation of p . Multiplying these equations by test functions, integrating over an element D_k of the layer Σ , and integrating by parts lead to the weak form

$$\begin{aligned} \left(\frac{\partial p_1}{\partial t}, \hat{p}_1 \right)_{D_k} - (\rho c^2 \mathbf{e}_1 (\mathbf{e}_1 \cdot \mathbf{u}), \nabla \hat{p}_1)_{D_k} + \langle f_{p_1}, \hat{p}_1 \rangle_{\partial D_k} &= (s_{p_1}, \hat{p}_1)_{D_k}, \\ \left(\frac{\partial p_2}{\partial t}, \hat{p}_2 \right)_{D_k} - (\rho c^2 \mathbf{e}_2 (\mathbf{e}_2 \cdot \mathbf{u}), \nabla \hat{p}_2)_{D_k} + \langle f_{p_2}, \hat{p}_2 \rangle_{\partial D_k} &= (s_{p_2}, \hat{p}_2)_{D_k}, \end{aligned}$$

where f^{p_1} and f^{p_2} are defined as

$$\begin{aligned} f_{p_1} &= \rho c^2 (\mathbf{n}_k \cdot \mathbf{e}_1) (\mathbf{e}_1 \cdot \mathbf{u}), \\ f_{p_2} &= \rho c^2 (\mathbf{n}_k \cdot \mathbf{e}_2) (\mathbf{e}_2 \cdot \mathbf{u}), \end{aligned}$$

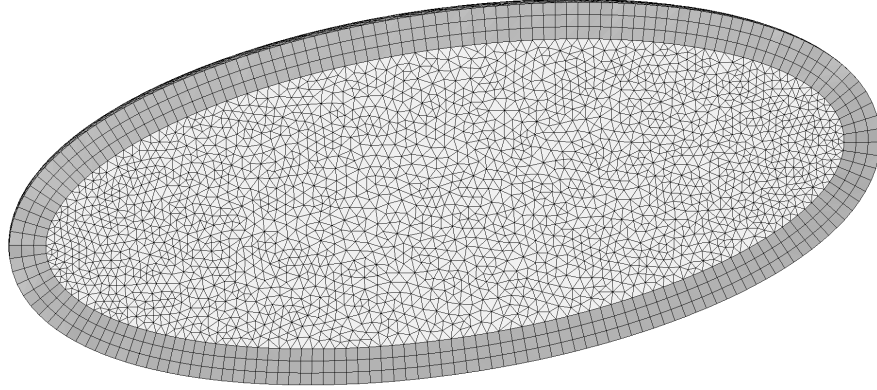


Figure 3: Geometry and mesh for the three-dimensional benchmark with a three-cells PML. This mesh is made of 58,396 tetrahedra in the truncated domain and $3 \times 6,998$ prisms in the layer.

and s_{p_1} and s_{p_2} contain the source terms written in the right-hand side of equations. Since system (13) is no longer strictly hyperbolic, we cannot use the Riemann solver to derive upwind fluxes. Noting the similitudes between f_p and both f_{p_1} and f_{p_2} , we propose to use the Lax-Friedrichs fluxes

$$\begin{aligned} f_{p_1}^{\text{num}} &= \rho c^2 (\mathbf{n}_k \cdot \mathbf{e}_1) (\mathbf{e}_1 \cdot \{\mathbf{u}\}) - c \llbracket p_1 \rrbracket, \\ f_{p_2}^{\text{num}} &= \rho c^2 (\mathbf{n}_k \cdot \mathbf{e}_2) (\mathbf{e}_2 \cdot \{\mathbf{u}\}) - c \llbracket p_2 \rrbracket. \end{aligned}$$

These fluxes are valid inside the layer Σ , but not at its external boundary Γ and at the interface Υ with the domain Ω . Indeed, because the supplementary fields are defined only inside the layer, we cannot use their semi-jumps $\llbracket p_1 \rrbracket$ and $\llbracket p_2 \rrbracket$ on Υ and Γ . Fortunately, we note that $\mathbf{n}_k = -\mathbf{e}_1$ on Υ and $\mathbf{n}_k = \mathbf{e}_1$ on Γ . We also have $\mathbf{n}_k \cdot \mathbf{e}_2 = 0$ on both surfaces. Therefore, we have $f_{p_1} = f_p$ and $f_{p_2} = 0$ in both cases. We then use the numerical flux f_p^{num} instead of $f_{p_1}^{\text{num}}$, and $f_{p_2}^{\text{num}}$ is simply set to zero.

Since the supplementary equations of the PML-ODE system (15) do not involve spatial differential operators, the derivation of the scheme is straightforward. In addition to the above scheme for the governing equations of p and \mathbf{u} , ordinary differential equations will be only local, at each node of each element, for the supplementary fields $p^{(1)}$, $p^{(2)}$, \mathbf{v} and \mathbf{w} . We use the same time-stepping scheme for both partial and ordinary differential equations.

3.2 Description of the benchmark

The computational domain Ω is the half of an ellipsoid, with axes of lengths 330 m (x -direction) and 120 m (y - and z -directions), respectively. A symmetry boundary condition is used in the section of the semi-ellipsoid, and the shell is extended with a PML Σ (Figure 3). To generate the wavefront, a Gaussian pulse is prescribed as initial condition on the pressure,

$$p(\mathbf{x}, 0) = e^{-r^2/R^2}$$

with $r = \|\mathbf{x} - \mathbf{x}_0\|$, $\mathbf{x}_0 = (-122.5 \text{ m}, 0 \text{ m}, 20 \text{ m})$ and $R = 7.5 \text{ m}$, while the other fields are initially set to zero. With this setting, the initial pressure is negligible inside the PML. We use the physical parameters $c = 1.5 \text{ km/s}$ and $\rho = 1 \text{ kg/m}^3$.

The mesh is made of tetrahedra in the truncated domain Ω and prisms in the layer Σ , with element sizes between 3 m and 5 m. The mesh of the layer is generated by extrusion. The main reason is that it can be automatically done for truncated domain of any shape with a regular enough boundary Υ . It does not require the analytic representation of the external boundary Γ of the layer. With an ellipsoidal domain, the external boundary Γ is not an ellipsoid (see *e.g.* [74]), and, to the best of our knowledge, no analytical representation is known. Ideally, a mesh with curvilinear elements should be used in order to exactly follow

the interface Υ and the boundary Γ that are curved. Elements with planar faces could be used with a lower computational cost, but the approximate polynomial representations of the surfaces introduce a geometric error. To reduce the global error, it is not clear if using curvilinear elements is computationally more efficient than using elements with planar faces and a thicker layer. In this paper, we consider only elements with planar faces.

We consider different thicknesses for the layer (1, 3 and 5 mesh cells) and both first-degree and second-degree basis functions. All the meshes are generated with Gmsh [33]. The time-stepping is made with the fourth-order Runge-Kutta scheme. The time step Δt is equal to 0.05 ms and 0.025 ms for first-degree and second-degree basis functions, respectively.

Two alternative absorption functions $\sigma(\xi_1)$ are considered: the hyperbolic function σ_h and the shifted hyperbolic function σ_{sh} , defined as

$$\begin{aligned}\sigma_h(\xi_1) &= \frac{c}{\delta - \xi_1}, \\ \sigma_{sh}(\xi_1) &= \frac{c}{\delta} \frac{\xi_1}{\delta - \xi_1}.\end{aligned}$$

It has been shown in previous works [16, 17, 57, 58] that both these functions do not require the tuning of parameters. In particular, we have shown [58] that σ_{sh} is a good choice for a discontinuous Galerkin implementation with a Cartesian PML formulation similar to the PML-PDE system (13). Here, both functions are tested with both PML systems (13) and (15).

The PML formulations require to know the coordinate ξ_1 , the principal curvatures κ_2 and κ_3 , and the local orthonormal frame $(\mathbf{e}_1, \mathbf{e}_2, \mathbf{e}_3)$. Both ξ_1 and \mathbf{e}_1 are computed numerically by finding, in the initialization of the simulation, the closest node belonging to the mesh of the surface Υ . To define the principal curvatures and the other vectors, we use the fact that the domain is an ellipsoid of revolution. Then, \mathbf{e}_2 belongs to the plane tangent to Υ and is oriented towards one pole, and \mathbf{e}_3 is perpendicular to both \mathbf{e}_2 and \mathbf{e}_1 . κ_2 corresponds to the curvature of an ellipse [76],

$$\kappa_2 = \frac{a_x a_y}{[p_x^2 (a_y/a_x)^2 + (p_y^2 + p_z^2) (a_x/a_y)^2]^{3/2}},$$

and κ_3 is obtained from the Gaussian curvature G of an ellipsoid [77],

$$G = \kappa_2 \kappa_3 = \frac{(a_x a_y a_z)^2}{[(p_x a_y a_z/a_x)^2 + (p_y a_x a_z/a_y)^2 + (p_z a_x a_y/a_z)^2]^2}.$$

In these formulas, a_x , a_y and a_z are the semi-axes of the ellipsoid and p_x , p_y and p_z are the Cartesian coordinates of $\mathbf{p}(\xi_2, \xi_3)$. Let us note that, in our case, $a_y = a_z$.

3.3 Validation and comparison

Figure 4 shows snapshots of the pressure p at different instants with a three-cells layer and the PML-PDE formulation. A spherical wave is generated by the initial pulse. As time goes by, the spherical wavefront reaches the PML with different angles of incidence, and propagates along the interface at a nearly grazing incidence. We observe that the spherical wave is not deformed near the interface, as we wished for, and the pressure is damped inside the layer.

The simulation is performed with different settings over the period [0 ms, 500 ms]. This includes a first phase where the wavefront is traveling in the truncated domain (before $t = 200$ ms) and a second phase where the wavefront has left the domain (after $t = 200$ ms). For all the settings, the difference between the numerical solution and the exact solution is quantified using the relative error defined as

$$\text{Error}(t) = \frac{\int_{\Omega} \left(\frac{1}{2\rho c^2} (p_{\text{exact}}(t, \mathbf{x}) - p_{\text{num}}(t, \mathbf{x}))^2 + \frac{\rho}{2} \|\mathbf{u}_{\text{exact}}(t, \mathbf{x}) - \mathbf{u}_{\text{num}}(t, \mathbf{x})\|^2 \right) d\mathbf{x}}{\int_{\Omega} \left(\frac{1}{2\rho c^2} (p_{\text{exact}}(0, \mathbf{x}))^2 + \frac{\rho}{2} \|\mathbf{u}_{\text{exact}}(0, \mathbf{x})\|^2 \right) d\mathbf{x}},$$

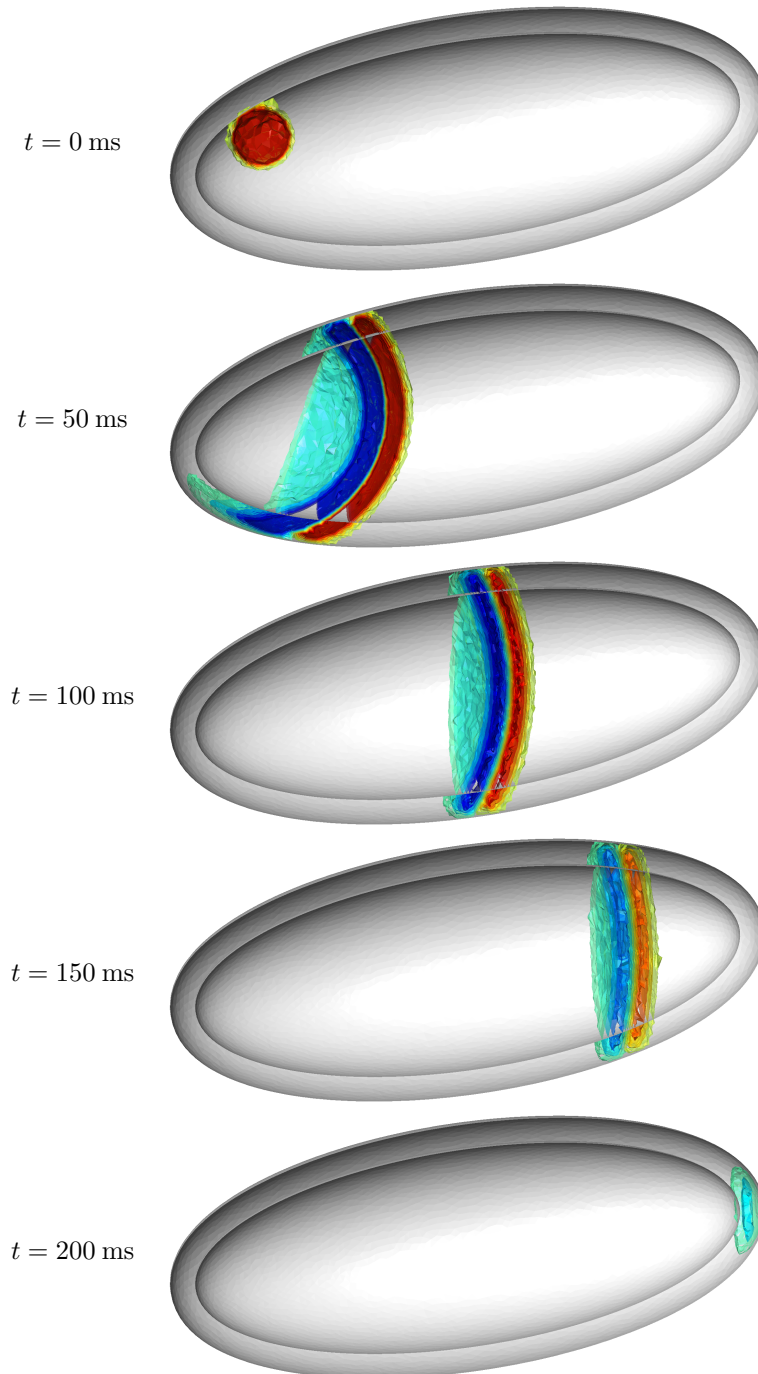


Figure 4: Snapshots of the solution of the three-dimensional benchmark at different instants. Colored surfaces are iso-surfaces of $p(\mathbf{x}, t)$. The inner and outer white surfaces correspond to the interior and exterior boundaries of the PML, respectively.

where the exact solution is given by

$$p_{\text{exact}}(t, \mathbf{x}) = \frac{1}{2} \left(\frac{r - ct}{r} e^{-(r-ct)^2/R^2} + \frac{r + ct}{r} e^{-(r+ct)^2/R^2} \right),$$

$$\mathbf{u}_{\text{exact}}(t, \mathbf{x}) = \frac{1}{2c\rho} \left[\left(\frac{R^2}{2r^2} + \frac{r - ct}{r} \right) e^{-(r-ct)^2/R^2} - \left(\frac{R^2}{2r^2} + \frac{r + ct}{r} \right) e^{-(r+ct)^2/R^2} \right] \frac{\mathbf{x} - \mathbf{x}_0}{r}.$$

The error corresponds to the ratio of the energy associated with the error fields to the energy associated with the initial fields in the truncated domain Ω .

Figure 5 shows the time-evolution of the error when the absorbing boundary condition (ABC) and three-cells PMLs are used as truncation technique. Both first-degree and second-degree basis functions are tested. During the period [0 ms, 200 ms], all the PMLs exhibit a similar error for each polynomial degree. This error dramatically decreases when increasing the degree from one to two. By contrast, the error corresponding to the ABC is larger and stays at the same level (between 10^{-2} and 10^{-1}) for both polynomial degrees. These observations are coherent with the properties of these truncation techniques. The considered ABC is only a first-order approximation that cannot simulate oblique outgoing waves without any reflection. The observed error then is dominated by the modeling error associated with spurious reflected waves already present at the continuous level. For the PMLs, the significant decay of error indicates that numerical errors dominate.

In the second phase of the simulation (after $t = 200$ ms), the ABC error curves are decreasing and similar with both polynomial degrees. The error is dominated by the modeling error corresponding to the multiple reflections of the initial wavefront that are leaving the domain. With the PMLs, the error curves are in a quite large range (between 10^{-7} and 10^{-5}) and have slightly different behaviors, which confirms that the kind of PML formulation and the absorption function impact the error. For both degrees, the error is far higher with the ABC than with the PMLs at the beginning of the second phase, but the ABC error goes under the error obtained with some PMLs at the end of the simulation. While the ABC error is dramatically decreasing during the second phase, the PML errors are only slightly decreasing or even slightly increasing.

This phenomenon could be explained by the linear growing modes that can be generated inside the PML and that can pollute the long-duration solution (see the end of section 3.3).

In order to compare the PML implementations, we now consider the mean value of the relative error over the period [250 ms, 500 ms], where the PMLs exhibit different errors. Figure 6 shows the mean error as function of the total runtime when using 2 Dual-Core Intel Xeon Processors L5420. All the one-cell PMLs provide similar errors for similar computational costs. For three-cells and five-cells layers, the PML-PDE implementation is more accurate with the shifted hyperbolic absorption function σ_{sh} than with the

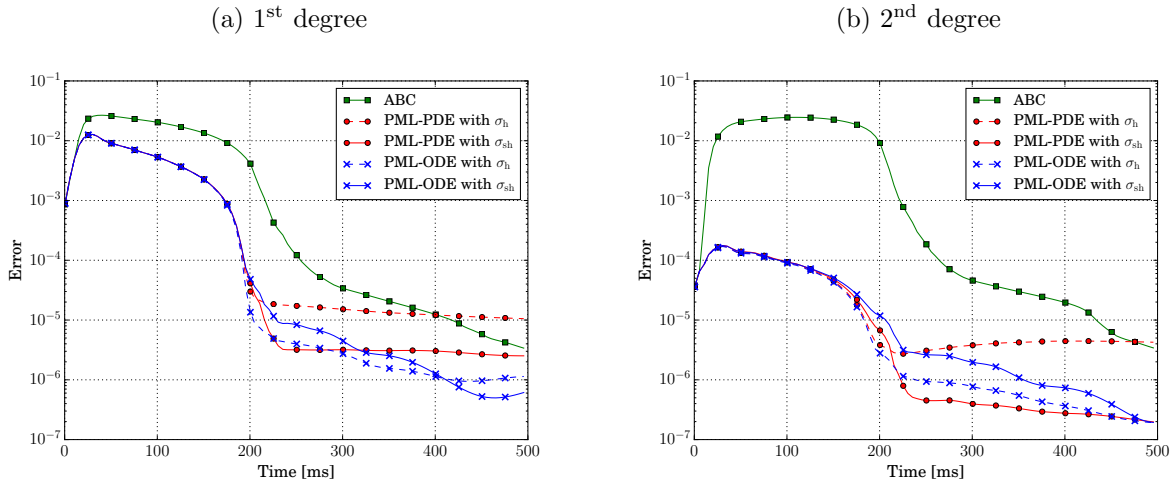


Figure 5: Time-evolution of the error inside the domain Ω with the absorbing boundary condition (ABC) and three-cells PMLs. First-degree (a) and second-degree (b) basis functions are considered with both PML formulations and both absorbing functions.

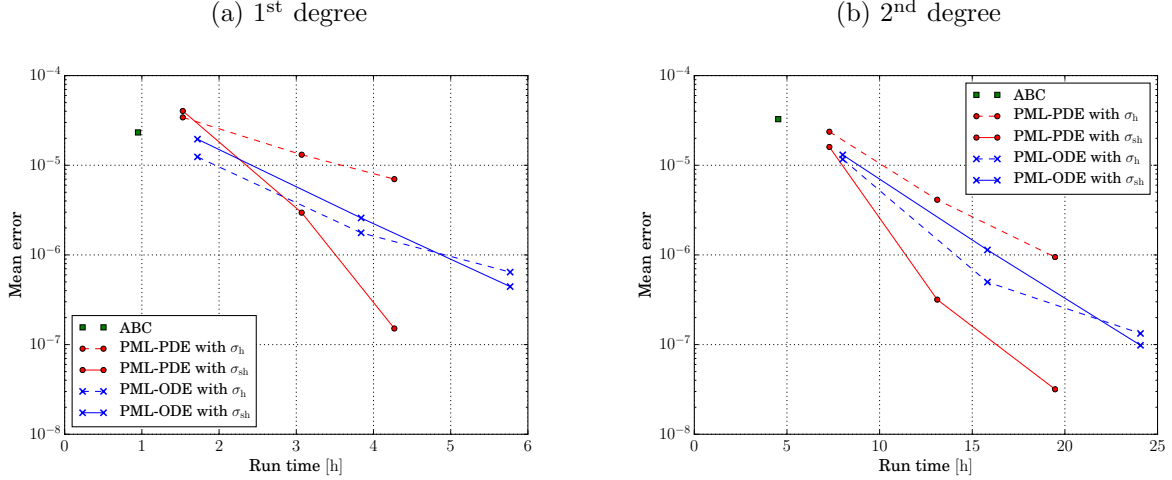


Figure 6: Mean error over the period [250 ms, 500 ms] as a function of the runtime. The three points of each curve correspond to one-cell (left), three-cells (middle) and five-cells (right) layers.

hyperbolic one σ_h . This result is coherent with the conclusions of previous works with similar formulations [57, 58]. For the PML-ODE implementation, both functions provide quite similar results. σ_h is slightly better than σ_{sh} with a three-cells layer, while the converse is true with a five-cells layer. Finally, the PML-PDE implementation (with the shifted hyperbolic function) is more efficient than the PML-ODE. For a five-cells layer, it even provides a more accurate result with a smaller runtime.

3.4 Illustration of application

Our strategy is now illustrated by the scattering of a submarine placed in the center of the ellipsoidal domain. The submarine is approximately 120 m in length, and the dimensions of the ellipsoid are not changed. The PML-PDE is used together with the shifted hyperbolic absorption function σ_{sh} and the first-order ABC to terminate the layer. The mesh is made of 183,707 tetrahedra (truncated domain) and 62,650 prisms (five-cells layer). First-degree basis functions are used. There are 7,450,112 degrees of freedom.

Figure 7 shows snapshots of the pressure p at different instants. The spherical wave generated by the initial pulse hits the front of the submarine, and creates perturbations in the pressure field. The wavefront propagates along the submarine and is nearly grazing at the boundary of the domain. The perturbations, as well as the primary spherical wave, have correctly left the front zone at $t = 200$ ms. These results have been obtained using 8 Dual-Core Intel Xeon Processors L5420. The total runtime was 1 h 40 min, corresponding to the period [0 ms, 200 ms] and to 8000 time steps.

4 Conclusion

This paper is dedicated to generalizing PML formulations for acoustic wave propagation with generally-shaped convex domains, which offers flexibility when choosing the shape of the computational domain. Our strategy is based on the complex stretch of a specific curvilinear coordinate in the time-harmonic equations, and on the use of supplementary differential equations to write the time-domain PML formulations.

Two time-dependent PML formulations have been derived for the pressure-velocity system. One formulation involves supplementary PDEs, while only ODEs are required for the other. Both have been implemented in a discontinuous Galerkin finite-element solver and tested with a three-dimensional benchmark. The best accuracy is observed with the PML-PDE formulation, despite an approximation made during the implementation. That formulation is faster than the other, but the complete version requires the knowledge of supplementary geometrical information. In a more applicative context, we believe that all the required

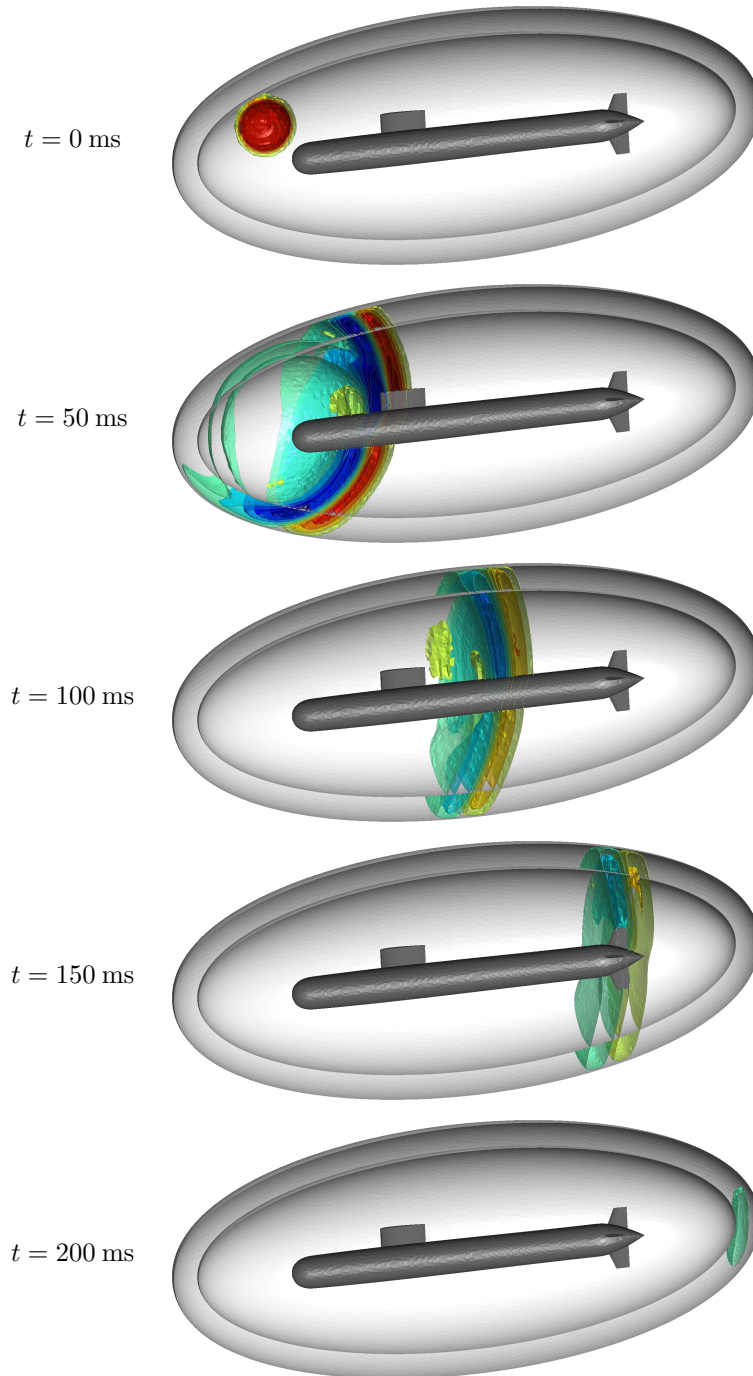


Figure 7: Snapshots of the solution of the three-dimensional benchmark at different instants. Colored surfaces are iso-surfaces of $p(\mathbf{x}, t)$. The inner and outer white surfaces correspond to the interior and exterior boundaries of the PML, respectively

geometrical parameters could be evaluated numerically or provided by the underlying CAD software in an automatic manner.

The approach is quite general and offers a wide range of extensions. Since the PML equations are written at the continuous level, they can be implemented with other numerical methods. As explained at the end of section 2.3, the formulations can be adapted to deal with domains having corners, though they have been derived assuming that the domain border was regular enough. The formulations can also be improved using a complex coordinate stretch with a frequency shift [50, 65].

Acknowledgements

This work was supported in part through the ARC grant for Concerted Research Actions (ARC WAVES 15/19-03), financed by the Wallonia-Brussels Federation, and by the Belgian Science Policy Office under grant IAP P7/02. Axel Modave was partially supported by an excellence grant from Wallonie-Bruxelles International (WBI). He was a Postdoctoral Researcher on leave with the F.R.S-FNRS. Jonathan Lambrechts was a Postdoctoral Researcher with the F.R.S-FNRS.

References

- [1] S. Abarbanel and D. Gottlieb. A mathematical analysis of the PML method. *Journal of Computational Physics*, 134(2):357–363, 1997.
- [2] S. Abarbanel and D. Gottlieb. On the construction and analysis of absorbing layers in CEM. *Applied Numerical Mathematics*, 27(4):331–340, 1998.
- [3] J. Alvarez, L. D. Angulo, A. R. Bretones, M. R. Cabello, and S. G. Garcia. A leap-frog discontinuous galerkin time-domain method for hif assessment. *IEEE Transactions on Electromagnetic Compatibility*, 55(6):1250–1259, 2013.
- [4] X. Antoine, H. Barucq, and A. Bendali. Bayliss-Turkel-like radiation conditions on surfaces of arbitrary shape. *Journal of Mathematical Analysis and Applications*, 229(1):184–211, 1999.
- [5] X. Antoine, A. Arnold, C. Besse, M. Ehrhardt, and A. Schädle. A review of transparent and artificial boundary conditions techniques for linear and nonlinear Schrödinger equations. *Communications in Computational Physics*, 4(4):729–796, 2008.
- [6] D. Appellö, T. Hagstrom, and G. Kreiss. Perfectly matched layers for hyperbolic systems: General formulation, well-posedness, and stability. *SIAM Journal on Applied Mathematics*, 67(1):1–23, 2006.
- [7] U. Basu and A. K. Chopra. Perfectly matched layers for time-harmonic elastodynamics of unbounded domains: theory and finite-element implementation. *Computer Methods in Applied Mechanics and Engineering*, 192(11-12):1337–1375, 2003.
- [8] U. Basu and A. K. Chopra. Perfectly matched layers for transient elastodynamics of unbounded domains. *International Journal for Numerical Methods in Engineering*, 59(8):1039–1074, 2004.
- [9] E. Bécache and P. Joly. On the analysis of Bérenger’s perfectly matched layers for Maxwell’s equations. *ESAIM: Mathematical Modelling and Numerical Analysis*, 36(1):87–119, 2002.
- [10] E. Bécache and A. Prieto. Remarks on the stability of cartesian PMLs in corners. *Applied Numerical Mathematics*, 62(11):1639–1653, 2012.
- [11] E. Bécache, S. Fauqueux, and P. Joly. Stability of perfectly matched layers, group velocities and anisotropic waves. *Journal of Computational Physics*, 188(2):399–433, 2003.
- [12] E. Bécache, P. G. Petropoulos, and S. D. Gedney. On the long-time behavior of unsplit perfectly matched layers. *IEEE Transactions on Antennas and Propagation*, 52(5):1335–1342, 2004.
- [13] J.-P. Bérenger. A perfectly matched layer for the absorption of electromagnetic waves. *Journal of Computational Physics*, 114(2):185–200, 1994.
- [14] J.-P. Bérenger. Three-dimensional perfectly matched layer for the absorption of electromagnetic waves. *Journal of Computational Physics*, 127(2):363–379, 1996.
- [15] J.-P. Bérenger. *Perfectly Matched Layer (PML) for Computational Electromagnetics*. Morgan & Claypool, 2007.
- [16] A. Bermúdez, L. Hervella-Nieto, A. Prieto, and R. Rodríguez. An exact bounded perfectly matched layer for time-harmonic scattering problems. *SIAM Journal on Scientific Computing*, 30(1):312–338, 2007.
- [17] A. Bermúdez, L. Hervella-Nieto, A. Prieto, and R. Rodríguez. An optimal perfectly matched layer with unbounded absorbing function for time-harmonic acoustic scattering problems. *Journal of Computational Physics*, 223(2):469–488, 2007.

- [18] A. Bermúdez, L. Hervella-Nieto, A. Prieto, and R. Rodríguez. Perfectly matched layers for time-harmonic second order elliptic problems. *Archives of Computational Methods in Engineering*, 17(1):77–107, 2010.
- [19] Z. Chen and X. Wu. Long-time stability and convergence of the uniaxial perfectly matched layer method for time-domain acoustic scattering problems. *SIAM Journal on Numerical Analysis*, 50(5):2632–2655, 2012.
- [20] W. C. Chew and Q. H. Liu. Perfectly matched layers for elastodynamics: A new absorbing boundary condition. *Journal of Computational Acoustics*, 4(4):341–359, 1996.
- [21] W. C. Chew and W. H. Weedon. A 3D perfectly matched medium from modified Maxwell’s equations with stretched coordinates. *Microwave and Optical Technology Letters*, 7(13):599–604, 1994.
- [22] W. C. Chew, J. M. Jin, and E. Michielssen. Complex coordinate stretching as a generalized absorbing boundary condition. *Microwave and Optical Technology Letters*, 15(6):363–369, 1997.
- [23] F. Collino and P. B. Monk. The perfectly matched layer in curvilinear coordinates. *SIAM Journal on Scientific Computing*, 19:2061–2090, 1998.
- [24] F. Collino and C. Tsogka. Application of the perfectly matched absorbing layer model to the linear elastodynamic problem in anisotropic heterogeneous media. *Geophysics*, 66(1):294–307, 2001.
- [25] T. Colonius. Modeling artificial boundary conditions for compressible flow. *Annual Review of Fluid Mechanics*, 36:315–345, 2004.
- [26] E. Demaldent and S. Imperiale. Perfectly matched transmission problem with absorbing layers: Application to anisotropic acoustics in convex polygonal domains. *International Journal for Numerical Methods in Engineering*, 96(11):689–711, 2013.
- [27] J. Diaz and P. Joly. A time domain analysis of PML models in acoustics. *Computer Methods in Applied Mechanics and Engineering*, 195(29):3820–3853, 2006.
- [28] M. P. Do Carmo. *Differential geometry of curves and surfaces*. Prentice-hall Englewood Cliffs, 1976.
- [29] B. Donderici and F. L. Teixeira. Conformal perfectly matched layer for the mixed finite element time-domain method. *IEEE Transactions on Antennas and Propagation*, 56(4):1017–1026, 2008.
- [30] S. Dosopoulos and J.-F. Lee. Interior penalty discontinuous Galerkin finite element method for the time-dependent first order Maxwell’s equations. *IEEE Transactions on Antennas and Propagation*, 58(12):4085–4090, 2010.
- [31] K. Duru. The role of numerical boundary procedures in the stability of perfectly matched layers. *SIAM Journal on Scientific Computing*, 38(2):A1171–A1194, 2016.
- [32] S. D. Gedney. An anisotropic perfectly matched layer-absorbing medium for the truncation of FDTD lattices. *IEEE Transactions on Antennas and Propagation*, 44(12):1630–1639, 1996.
- [33] C. Geuzaine and J.-F. Remacle. Gmsh: A 3-D finite element mesh generator with built-in pre-and post-processing facilities. *International Journal for Numerical Methods in Engineering*, 79(11):1309–1331, 2009.
- [34] D. Givoli. *Numerical Methods for Problems in Infinite Domains*. Elsevier, 1992.
- [35] D. Givoli. High-order local non-reflecting boundary conditions: a review. *Wave Motion*, 39(4):319–326, 2004.
- [36] D. Givoli. Computational absorbing boundaries. In *Computational Acoustics of Noise Propagation in Fluids*, chapter 5, pages 145–166. Springer, Berlin, 2008.
- [37] M. N. Guddati and K.-W. Lim. Continued fraction absorbing boundary conditions for convex polygonal domains. *International Journal for Numerical Methods in Engineering*, 66(6):949–977, 2006.
- [38] T. Hagstrom. Radiation boundary conditions for the numerical simulation of waves. *Acta Numerica*, 8:47–106, 1999.
- [39] T. Hagstrom. Radiation boundary conditions for Maxwell’s equations: a review of accurate time-domain formulations. *Journal of Computational Mathematics*, 25:305–336, 2007.
- [40] T. Hagstrom, D. Givoli, D. Rabinovich, and J. Bielak. The double absorbing boundary method. *Journal of Computational Physics*, 259(0):220–241, 2014.
- [41] L. Halpern and J. Rauch. Hyperbolic boundary value problems with trihedral corners. *AIMS series in Applied Mathematics*, 2016.
- [42] L. Halpern, S. Petit-Bergez, and J. Rauch. The analysis of matched layers. *Confluentes Mathematici*, 3(02):159–236, 2011.
- [43] F. D. Hastings, J. B. Schneider, and S. L. Broschat. Application of the perfectly matched layer (PML) absorbing boundary condition to elastic wave propagation. *The Journal of the Acoustical Society of America*, 100:3061, 1996.
- [44] J. S. Hesthaven and T. Warburton. *Nodal discontinuous Galerkin methods: algorithms, analysis, and applications*, volume 54. Springer-Verlag New York, 2008.
- [45] F. Q. Hu. On absorbing boundary conditions for linearized euler equations by a perfectly matched layer. *Journal of Computational Physics*, 129(1):201–219, 1996.
- [46] F. Q. Hu. Development of PML absorbing boundary conditions for computational aeroacoustics: A progress review. *Computers & Fluids*, 37(4):336–348, 2008.
- [47] F. Q. Hu, X. D. Li, and D. K. Lin. Absorbing boundary conditions for nonlinear Euler and Navier-Stokes

- equations based on the perfectly matched layer technique. *Journal of Computational Physics*, 227(9):4398–4424, 2008.
- [48] B. Kaltenbacher, M. Kaltenbacher, and I. Sim. A modified and stable version of a perfectly matched layer technique for the 3-d second order wave equation in time domain with an application to aeroacoustics. *Journal of Computational Physics*, 235:407–422, 2013.
- [49] D. Katz, E. Thiele, and A. Taflove. Validation and extension to three dimensions of the Bérenger PML absorbing boundary condition for FD-TD meshes. *IEEE Microwave and Guided Wave Letters*, 4(8):268–270, 1994.
- [50] M. Kuzuoglu and R. Mittra. Frequency dependence of the constitutive parameters of causal perfectly matched anisotropic absorbers. *IEEE Microwave and Guided Wave Letters*, 6(12):447–449, 1996.
- [51] M. Lassas and E. Somersalo. Analysis of the PML equations in general convex geometry. *Proceedings of the Royal Society of Edinburgh: Section A Mathematics*, 131:1183–1207, 2001.
- [52] M. Lassas, J. Liukkonen, and E. Somersalo. Complex Riemannian metric and absorbing boundary condition. *Journal de Mathématique Pures et Appliquées*, 80(7):739–768, 2001.
- [53] J. W. Lavelle and W. C. Thacker. A pretty good sponge: Dealing with open boundaries in limited-area ocean models. *Ocean Modelling*, 20(3):270–292, 2008.
- [54] R. J. LeVeque. *Finite volume methods for hyperbolic problems*, volume 31. Cambridge University Press, 2002.
- [55] P. J. Matuszyk and L. F. Demkowicz. Parametric finite elements, exact sequences and perfectly matched layers. *Computational Mechanics*, 51(1):35–45, 2013.
- [56] K. Meza-Fajardo and A. Papageorgiou. A nonconvolutional, split-field, perfectly matched layer for wave propagation in isotropic and anisotropic elastic media: Stability analysis. *Bulletin of the Seismological Society of America*, 98(4):1811–1836, 2008.
- [57] A. Modave, A. Kamenii, J. Lambrechts, E. Delhez, L. Pichon, and C. Geuzaine. An optimum PML for scattering problems in the time domain. *The European Physical Journal Applied Physics*, 64, 11 2013.
- [58] A. Modave, E. Delhez, and C. Geuzaine. Optimizing perfectly matched layers in discrete contexts. *International Journal for Numerical Methods in Engineering*, 99(6):410–437, 2014.
- [59] F. Nataf. A new approach to perfectly matched layers for the linearized Euler system. *Journal of Computational Physics*, 214(2):757–772, 2006.
- [60] I. M. Navon, B. Neta, and M. Y. Hussaini. A perfectly matched layer approach to the linearized shallow water equations models. *Monthly Weather Review*, 132(6):1369–1378, 2004.
- [61] P. G. Petropoulos. Reflectionless sponge layers as absorbing boundary conditions for the numerical solution of Maxwell equations in rectangular, cylindrical, and spherical coordinates. *SIAM Journal on Applied Mathematics*, 60(3):1037–1058, 2000.
- [62] A. N. Rahmouni. An algebraic method to develop well-posed PML models: Absorbing layers, perfectly matched layers, linearized Euler equations. *Journal of Computational Physics*, 197(1):99–115, 2004.
- [63] C. Rappaport. Interpreting and improving the PML absorbing boundary condition using anisotropic lossy mapping of space. *IEEE Transactions on Magnetics*, 32(3):968–974, 1996.
- [64] J. A. Roden and S. D. Gedney. Efficient implementation of the uniaxial-based PML media in three-dimensional nonorthogonal coordinates with the use of the FDTD technique. *Microwave and Optical Technology Letters*, 14(2):71–75, 1997.
- [65] J. A. Roden and S. D. Gedney. Convolutional PML (CPML): An efficient FDTD implementation of the CFS-PML for arbitrary media. *Microwave and Optical Technology Letters*, 27(5):334–338, 2000.
- [66] Z. S. Sacks, D. M. Kingsland, R. Lee, and J.-F. Lee. A perfectly matched anisotropic absorber for use as an absorbing boundary condition. *IEEE Transactions on Antennas and Propagation*, 43(12):1460–1463, 1995.
- [67] K. Schmidt, J. Diaz, and C. Heier. Non-conforming Galerkin finite element methods for local absorbing boundary conditions of higher order. *Computers & Mathematics with Applications*, 70(9):2252–2269, 2015.
- [68] F. Teixeira, K.-P. Hwang, W. Chew, and J.-M. Jin. Conformal PML-FDTD schemes for electromagnetic field simulations: A dynamic stability study. *IEEE Transactions on Antennas and Propagation*, 49(6):902–907, 2001.
- [69] F. L. Teixeira and W. C. Chew. PML-FDTD in cylindrical and spherical grids. *IEEE Microwave and Guided Wave Letters*, 7(9):285–287, 1997.
- [70] F. L. Teixeira and W. C. Chew. Systematic derivation of anisotropic PML absorbing media in cylindrical and spherical coordinates. *IEEE Microwave and Guided Wave Letters*, 7(11):371–373, 1997.
- [71] F. L. Teixeira and W. C. Chew. Analytical derivation of a conformal perfectly matched absorber for electromagnetic waves. *Microwave and Optical Technology Letters*, 17(4):231–236, 1998.
- [72] F. L. Teixeira and W. C. Chew. Unified analysis of perfectly matched layers using differential forms. *Microwave and Optical Technology Letters*, 20(2):124–126, 1999.
- [73] F. L. Teixeira and W. C. Chew. Differential forms, metrics, and the reflectionless absorption of electromagnetic waves. *Journal of Electromagnetic Waves and Applications*, 13(5):665–686, 1999.
- [74] F. L. Teixeira and W. C. Chew. Complex space approach to perfectly matched layers: a review and some new developments. *International Journal of Numerical Modelling-Electronic Networks Devices and Fields*, 13

- (5):441–455, 2000.
- [75] S. V. Tsynkov. Numerical solution of problems on unbounded domains. A review. *Applied Numerical Mathematics*, 27(4):465–532, 1998.
- [76] E. W. Weisstein. Ellipse. <http://mathworld.wolfram.com/Ellipse.html>, From MathWorld – A Wolfram Web Resource, 2015.
- [77] E. W. Weisstein. Ellipsoid. <http://mathworld.wolfram.com/Ellipsoid.html>, From MathWorld – A Wolfram Web Resource, 2015.
- [78] L. Zhao and A. C. Cangellaris. GT-PML: Generalized theory of perfectly matched layers and its application to the reflectionless truncation of finite-difference time-domain grids. *IEEE Transactions on Microwave Theory and Techniques*, 44(12):2555–2563, 1996.
- [79] C. Zheng. A perfectly matched layer approach to the nonlinear Schrödinger wave equations. *Journal of Computational Physics*, 227(1):537–556, 2007.
- [80] L. Zschiedrich, R. Klose, A. Schädle, and F. Schmidt. A new finite element realization of the perfectly matched layer method for Helmholtz scattering problems on polygonal domains in two dimensions. *Journal of Computational and Applied Mathematics*, 188(1):12–32, 2006.